



Construction and Building Materials

Volume 184, 30 September 2018, Pages 151–164



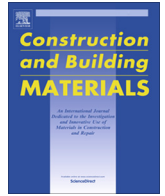
Probabilistic seismic performance evaluation of steel moment frame using high-strength and high-ductility steel

Kuo-Wei Liao ^a , Yu-I Wang ^b, Cheng-Cheng Chen ^c



Contents lists available at ScienceDirect

Construction and Building Materials

journal homepage: www.elsevier.com/locate/conbuildmat

Probabilistic seismic performance evaluation of steel moment frame using high-strength and high-ductility steel

Kuo-Wei Liao^{a,*}, Yu-I Wang^b, Cheng-Cheng Chen^c^a Department of Bioenvironmental Systems Engineering, National Taiwan University, Taipei 106, Taiwan^b CTCI Corporation, Taipei, Taiwan^c Department of Civil & Construction Engineering, National Taiwan University of Science & Technology, Taiwan

H I G H L I G H T S

- Using ductile and high-strength steels, a damaged-controlled frame is designed.
- Kinematic hardening and two surface theories are coded as an ABAQUS UMAT for BRB.
- A design recommendation is provided for engineers based on the optimal structure.
- The economic feasibility of using high-strength steel in a frame is revealed.

A R T I C L E I N F O

Article history:

Received 18 May 2016

Received in revised form 6 January 2018

Accepted 23 June 2018

Keywords:

High strength steel

High ductility steel

UMAT

Kinematic hardening

Two surfaces

A B S T R A C T

To shorten a steel building recovery time after an earthquake, a dual and damaged-controlled system is proposed, in which the seismic energy is absorbed by a highly ductile buckling restrained brace (BRB) and the gravity load is resisted by high-strength column. Because the seismic energy is mainly dissipated by the BRB, to accurately simulate the BRB hysteretic behavior is essential. Thus, kinematic hardening and two surface theories are adopted and coded as an ABAQUS user-defined material (UMAT). Particle swarm optimization (PSO) is used to find the optimal design equivalent to a corresponding traditional structure. The performance of the optimal frame is verified by nonlinear time history and fragility analysis. Based on the found optimum, a practical design guideline is recommended. The performance of high-strength steel and a high-ductility structural system such as the inter-story drift, maximum roof acceleration, property of BRB hysteresis, strength ratio between the main frame and BRB and cumulative fatigue damage are investigated. In addition, the economic feasibility of using high-strength steel in the structural system is compared to that using traditional steel materials.

© 2018 Elsevier Ltd. All rights reserved.

1. Introduction

A dual system is often employed in designing a building to reduce the seismic damage potential. The dual system consists of two major components: non-dissipative and dissipative members. Based on this concept, many different designs have been developed. For example, Zhang and Zirakian [1] employed low yield point (LYP) steel plate shear walls (SPSWs) as the primary dissipative members in moment resisting frames resulting in a better seismic performance. Tenchini et al. [2] proposed using high-strength steel (HSS) in non-dissipative members and mild carbon steel (MCS) in dissipative zones. Perri et al. [3] investigated the cost and low-cycle fatigue characteristics of Y-shaped steel bracing that

is often adopted for retrofitting buildings in medium-to-low seismic intensity area. Marshall and Charney [4] studied the seismic response of steel frame structures using a hybrid passive control system. Experimental and numerical studies of buckling restrained braces (BRB) have revealed that BRB, all-steel or concrete filled, is an effective dissipative structural member [5,6]. The performance of high- and low-strength steel in a moment frame has drawn much attention and is the focus of the current study. To be specific, this study addresses HT690, SN490 and A36 for use in building construction and includes a probabilistic seismic assessment. The performance of the aforementioned hybrid structure under seismic excitations is investigated and compared to that of a building constructed from traditional steel having normal yield strength. The motivation of using such a hybrid structure is that yield occurs only in the dissipative components, and through the quick-recovery characteristic of the dissipating

* Corresponding author.

E-mail address: kliao@ntu.edu.tw (K.-W. Liao).

system, structures are restored to their original function in the shortest time possible.

Because the majority of seismic energy is absorbed by the BRB, accuracy in modeling the hysteretic behavior of BRB is essential. Budaházy and Dunai [5] emphasized that the behavior of the BRB is complex. Instead of being numerically simulated, it is often studied by experimental tests. For example, Chen et al. [7] conducted cyclic loading tests with low yield steel (LYS 100) as the main load-bearing element of the BRB and combined the BRB with ductile concentrically braced frames (DCBF) for a reduced-size structure shaking table test. This combination aims to achieve a lower strength ratio in the main frame system and a higher strength ratio in the braces to ensure that plastic deformation occurs on the BRB. The strength ratio is the quotient of the strength demand (e.g., flexural and shear) from external force to the strength capacity provided by the considered structural member. The results indicate that compared to traditional braces, the BRB provides relatively good strength capacity, ductility and energy dissipation behavior, the DCBF exhibits good seismic behavior and the BRB reduces structure acceleration response and provides effective control in terms of the inter-story drift after yielding. The inter-story drift is a ratio of the relative translational displacement between two consecutive stories to height of that floor. Although much BRB research has been conducted through experiments, some numerical models have been proposed. For example, OpenSees provides a material called Steel BRB that can be used to investigate the hysteretic properties of BRB core material [8]. Cofie and Krawinkler [9] used a bounding surface model based on monotonic and cyclic stress-strain curves to simulate the nonlinear behavior of structural steel. In their model, the upper and lower stress bounds are controlled by hardening, softening, and mean stress relaxation, the strain amplitude of the last excursion and the previous stress-strain history. Wang [10] adopted the bounding surface model developed by Cofie and Krawinkler [9] to establish an all-steel BRB hysteretic model under a DRAIN-2D environment, in which three different steel materials, LYS, A572Gr.50 and TMCP, were used as the main load-bearing elements of BRB. The bounding surface model was also adopted by Ling et al. [11] to simulate the mechanical behavior of geosynthetic reinforcements that often exhibit large plastic strains, highly nonlinear and hysteretic behaviors under cyclic loading.

To accurately describe the nonlinear behavior of BRB subjected to seismic excitations, this study develops a uniaxial equivalent constitutive model that incorporates strain softening and hardening. The hysteretic model is constructed based on experimental results of monotonic and cyclic stress-strain curves and implemented in ABAQUS through its user subroutine interface - user-defined material (UMAT). After calibration, the established UMAT is applied to BRB members of steel moment frames for nonlinear time history analysis.

The structural members of the hybrid frame are minimized using particle swarm optimization (PSO) with performance constraints to ensure it is equivalent to that of the dual moment frame using normal strength steel. A probabilistic seismic performance evaluation and a fragility analysis are conducted for the optimal frame, and the performance measurements of interest in this study are the inter-story drift, maximum roof acceleration, BRB hysteretic behavior, strength ratio between main frame and BRB and cumulative fatigue damage. In addition to the structural performance, the economic feasibility of using high-strength steel in the structural system is also compared to that of using traditional steel materials. Based on these research results, this study provides a design guideline that includes the strength ratio values for column, beam and brace to leverage the results of the adopted optimization process and streamline the design process. Because the non-linear behavior of the structure system mainly occurs in the

BRB members, the common beam element with potential plastic hinges at two ends is adopted to simulate the main structure frame system. The details of this study are provided below.

2. BRB tests and test results

The Structural Engineering Laboratory, Department of Civil and Construction Engineering, National Taiwan University of Science and Technology successively completed over 40 large-size all-steel BRB load-bearing tests [7]. The main load-bearing elements of the test specimens ranged from 10 to 20 mm in thickness and approximately 2800 mm in length and are tested through displacement-controlled cyclic loading. The main load-bearing elements are fabricated from LYP, A36, A572 Gr. 50 and SM570 steel. The details of a tested BRB and test arrangement of the BRB specimens are shown in Fig. 1. The loading cycle is divided into two groups (LV and LC). The LV loading group used a gradual increment of displacement amplitude as shown in Fig. 2, and its results can provide the necessary statistics for establishing the hysteretic model. The LC series specimens, in contrast, used a fixed displacement amplitude to provide the parameters needed to

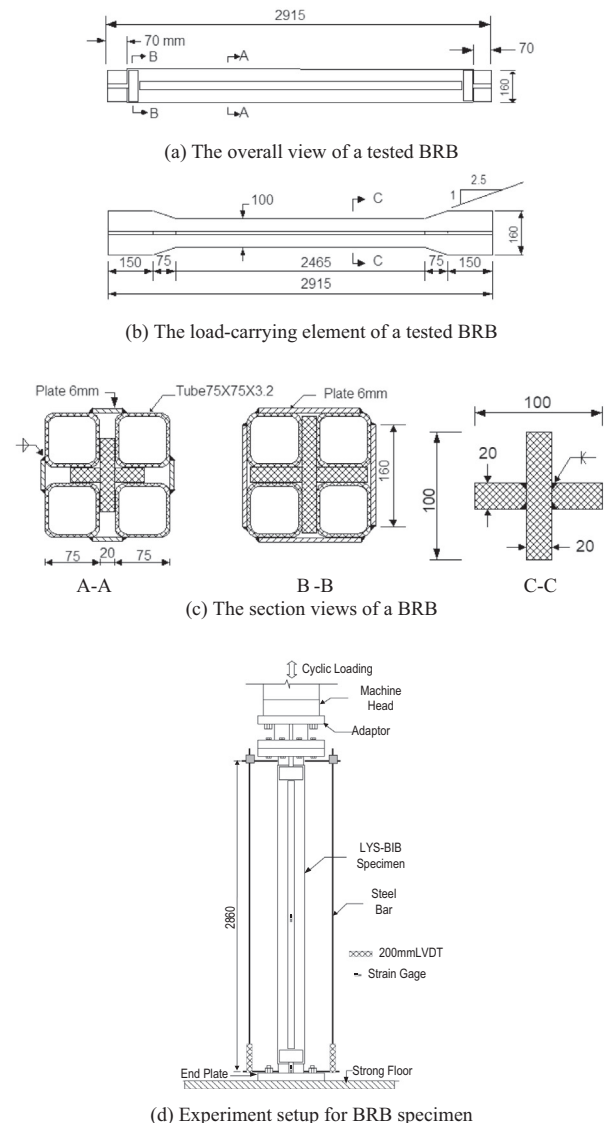


Fig. 1. (a) The overall view of a BRB (b) The load-carrying element of a BRB (c) The section views of a BRB (d) Experiment setup for BRB specimen.

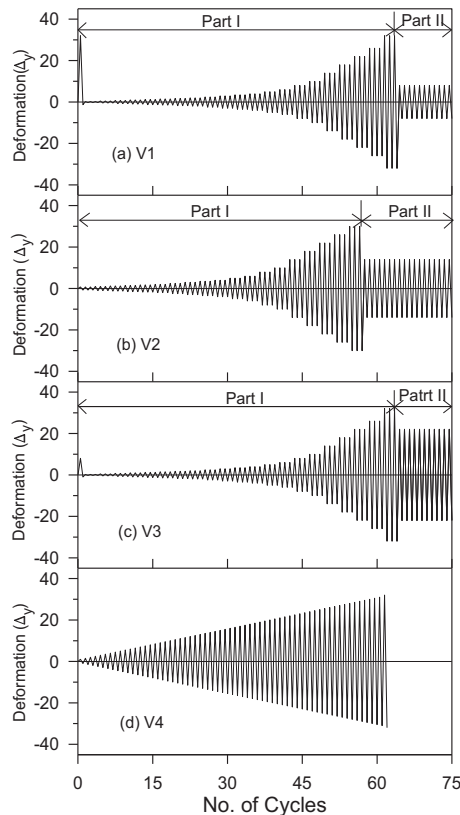


Fig. 2. LV1 to LV4 loading cycles.

establish the fatigue life. The displacement amplitudes for LC1 to LC6 were $\pm 2\Delta_y$, $\pm 4\Delta_y$, $\pm 8\Delta_y$, $\pm 11\Delta_y$, $\pm 16\Delta_y$ and $\pm 32\Delta_y$; among these, $y = 1.25$ mm was the yield displacement for the LYS-BRB element.

Fig. 3 shows the load-displacement hysteresis loops for the LV group specimens. A total of 941, 163, 89 and 63 cycles were completed for specimens from LV1 to LV4, respectively. Fig. 3 shows the stable hysteresis loops generated by LYS-BRB. No strength degradation occurred before failure; the specimen exhibited strain hardening with increasing displacement load. In addition, the hysteresis loops are saturated without displaying pinching, and there

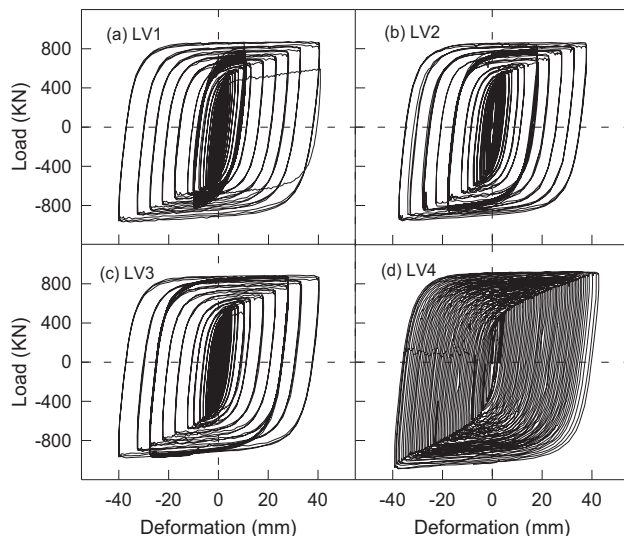


Fig. 3. Hysteresis loops of specimens subjected to LV1 to LV4.

is no significant degradation between the hysteresis loops. All specimens exhibited stable increase in strength after the yield point and the yield potential was considered favorable.

A total of 14,337 displacement cycles were completed for LC1 ($\pm 2\Delta_y$), but the displacement cycles decreased with increasing displacement amplitude. For example, only 18 displacement cycles were completed for LC6 ($\pm 32\Delta_y$). All of the testing results for LC specimen are displayed in Table 1. With information revealed in Table 1, the strain fatigue curve can be built based on the “BRB damage index” section. Fig. 4 shows the hysteresis loops of partial LC specimens. It can be observed that energy dissipation in each cycle increases as the number of displacement loops increases as a result of strain hardening behavior. The most significant strain hardening phenomenon was detected in the first three cycles, but the phenomenon was attenuated in later cycles. For example, for the load at LC2 ($\pm 2\Delta_y$) (Fig. 4(a)) the maximum load in the first cycle is +512 kN and is 555 kN in the last cycle. The differential is 43 kN. For the load at LC5 ($\pm 16\Delta_y$) (Fig. 4(c)) the maximum load in

Table 1

The detailed testing results of LC series.

Test name	Loading condition	Cycles at failure	Absorbed energy	Max. tension	Max. compression
LC1	$\pm 2\Delta_y$	14,337	31,296	441	436
LC2	$\pm 4\Delta_y$	3899	25,962	594	599
LC3	$\pm 8\Delta_y$	1084	18,754	698	764
LC4	$\pm 11\Delta_y$	714	20,490	768	813
LC5	$\pm 16\Delta_y$	115	4147	828	838
LC6	$\pm 32\Delta_y$	18	1859	906	1022

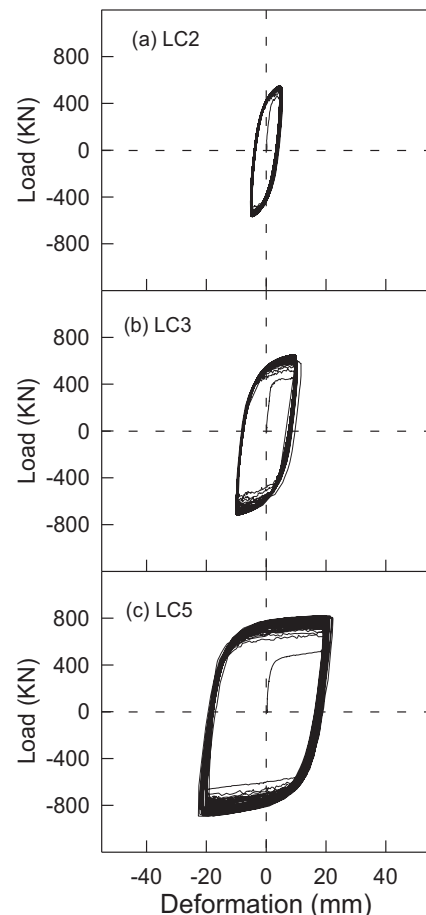


Fig. 4. Hysteresis loops of specimens subjected to LC2, LC3 and LC5.

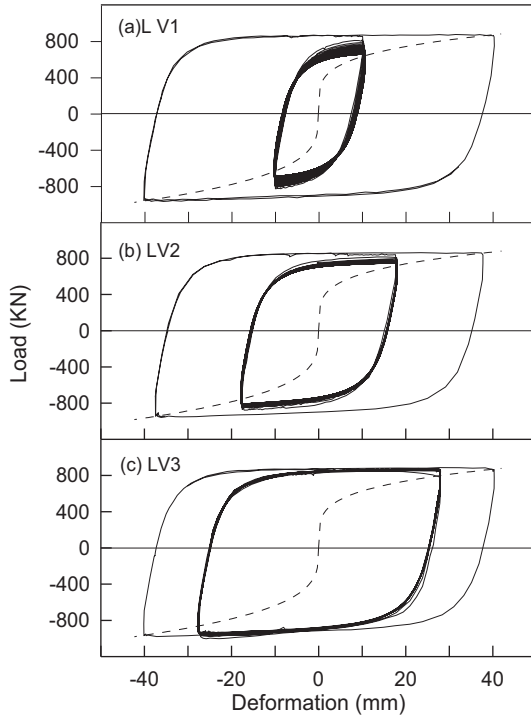


Fig. 5. Softening phenomenon of specimens subjected to LV1, LV2 and LV3.

the first cycle is +648 kN and is 828 kN in the last cycle. The differential is 180 kN. Fig. 5 shows the hysteresis loops of LV1, LV2 and LV3 specimens from part I to part II loading cycles. As shown in Fig. 2, the load of LV1 in the second stage dropped from $30\Delta_y$ to $8\Delta_y$ (from the 64th to 941st cycle), LV2 from $32\Delta_y$ to $14\Delta_y$ (the 57th to 163rd cycle) and LV3 from $32\Delta_y$ to $22\Delta_y$ (the 64th to 89th cycle). The maximum load of all three specimens decreased with an increasing number of displacement cycles when entering the part II phase, and strain softening was detected. The strain softening phenomenon is less obvious when the displacement decrease is smaller (LV3 in Fig. 5) and more obvious when the displacement decrease is larger (LV1 Fig. 5). The dotted lines in Fig. 5 are skeleton curves. Fig. 5 indicates that the strain softening phenomenon caused the maximum load of each loop to lean toward the skeleton curve as the number of loops increased, but the maximum load of each loop did not meet the skeleton curve. The maximum load of LV1, LV2 and LV3 exceeded the skeleton curves by 15, 11 and 5%, respectively, after strain softening.

3. BRB mathematical model, ABAQUS UMAT and damage index

All-steel BRB exhibits stable hysteresis loops and, as displacement increases, the strain hardening phenomenon becomes more obvious. When the displacement decreases, strain softening becomes clearly detectable. In addition, the yielding stress shifts because of the displacement change as shown in Figs. 3–5. To accurately simulate these BRB behaviors, the bounding surfaces method and kinematic hardening model are adopted based on the results of monotonic and cyclic experiments. For example, the cyclic test is used to construct the skeleton curve that is one of the major factors determining the locations of stress bounds, and the monotonic test can be used to determine the initial yielding stress. Existing finite element software often does not replicate this mechanical behavior. Therefore, this study develops a nonlinear user defined material provided in ABAQUS to simulate BRB hysteresis behaviors. The details of establishing UMAT are described below.

3.1. Bounding surfaces model

Although strain hardening and softening phenomena are observed, the mean stress relaxation is not significant and is not considered in this study. The two bounding surfaces method is described as follows.

1. Determination of the skeleton curve: the stresses (in MPa) on skeleton curves for different materials are obtained using regression analysis as shown in Eqs. (1)–(4).

LYS:

$$\sigma = 32.186 \times \ln(\varepsilon) + 363.35, \text{ in tension} \quad (1)$$

$$\sigma = 35.055 \times \ln(\varepsilon) + 391.36, \text{ in compression} \quad (2)$$

A36:

$$\begin{cases} \sigma = 143700 \times (\varepsilon) & \text{for } \varepsilon < 0.00242 \\ \sigma = 2857 \times (\varepsilon) + 348 & \text{for } \varepsilon > 0.00242 \text{ in tension} \end{cases} \quad (3)$$

$$\begin{cases} \sigma = 161667 \times (\varepsilon) & \text{for } \varepsilon < 0.00242 \\ \sigma = 6455 \times (\varepsilon) + 348 & \text{for } \varepsilon > 0.00242 \text{ in compression} \end{cases} \quad (4)$$

2. Determination of the initial stress bounds: The initial values of the upper and lower bounds are set as σ_y with a slope of $0.05E$, where σ_y is the yield stress and E is the elastic Young's modulus.
3. Calculation of the strain-hardening parameter (E_p^n): E_p^n is calculated using Eq. (5)

$$E_p^n = E_p^0 + (E - E_p^0) \times \left(\frac{\delta}{\delta_{in}} \right)^2 \quad (5)$$

in which E_p^0 is the initial strain-hardening parameter equal to $0.05E$ and E_p^n is the updated strain-hardening parameter. The definitions of δ_{in} , E_p^0 and E_p^n are provided in Fig. 6.

4. Updating the upper and lower stress bounds: Based on Coffie and Krawinkler [9], the stress bounds are updated based on the strain (ε_a) and stress (σ_a) of the last excursion and the stress (σ_s) on the skeleton curve corresponding to ε_a . If σ_a is smaller than σ_s , the next loading cycle will be accompanied by strain hardening and the upper and lower bounds will increase to $2\Delta s F_h$, in which $\Delta s = |\sigma_a - \sigma_s|$ and F_h is the hardening coefficient. In contrast, if σ_a is larger than σ_s , the next loading cycle will be accompanied by strain softening. These two stress bounds are continuously modified during the loading process.

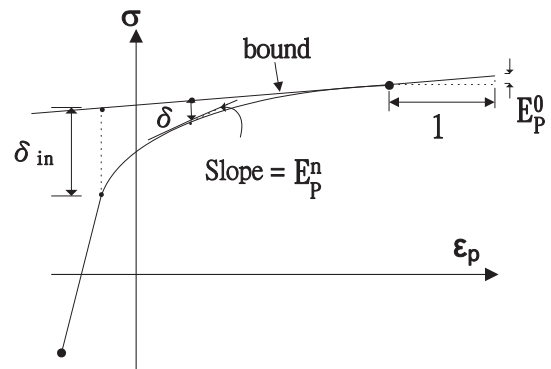


Fig. 6. Parameters used in the proposed Hysteresis curve.

3.2. ABAQUS UMAT and simulation results

The aforementioned BRB model is formulated as an ABAQUS UMAT. Prior to each ABAQUS load increment, the UMAT subroutine is executed to provide the necessary information such as the element contribution $[K_e]$ to the global stiffness matrix $[K]$ and the element solution-dependent state variables (e.g., the plastic energy dissipation). The ABAQUS main program starts the next increment if the resulting structural load has converged to the applied load in the current load increment. The calculation flow chart of the UMAT applied in BRB is described in Fig. 7. The responses of ABAQUS BRB

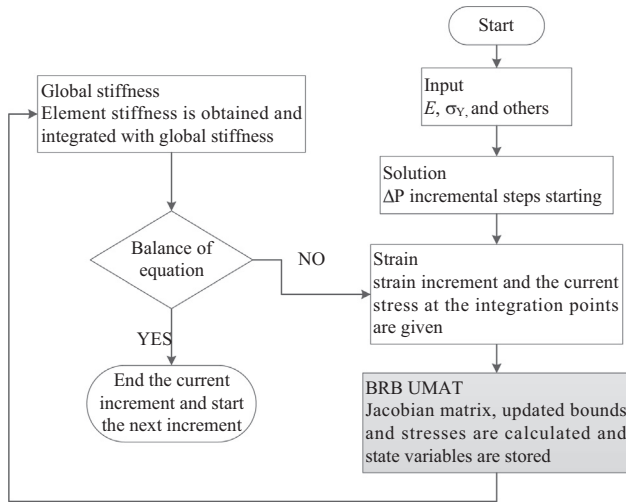


Fig. 7. The built BRB UMAT in ABAQUS calculation.

subjected to loadings of LV1 ~ LV4 are displayed in Fig. 8. Comparing to the experimental results as shown in Fig. 3, a very promising outcome is identified.

3.3. BRB damage index

The failure of BRB has been identified as a low-cycle fatigue [10]. Thus, a strain fatigue curve similar to the stress fatigue curve of the high-cycle fatigue is then established based on test results of LC cyclic loadings, as shown in Eq. (6).

$$\Delta \varepsilon_p = \varepsilon_f (2N_f)^c \quad (6)$$

in which $\Delta \varepsilon_p$ is the range of plastic strain, $2N_f$ represents the number of cycles that causes fatigue failure and ε_f and c are regression parameters. Because the loading sequence in low-cycle fatigue is not as important as in high-cycle fatigue, this study adopts Miner [12] to establish the linear cumulative damage index for BRB, as shown in Eq. (7):

$$D = \sum_i^k \frac{n_i}{N_{fi}} = \frac{n_1}{N_{f1}} + \frac{n_2}{N_{f2}} + \dots + \frac{n_k}{N_{fk}} \quad (7)$$

in which n_i is the number of cycles of strain i , N_{fi} is the number of cycles for fatigue failure when a constant strain of i is applied, and if D is greater than 1, the BRB has reached fatigue damage. Eqs. (8) and (9) are strain fatigue curves of LYS all-steel BRB established through regression based on the test results.

$$N = 3.8 \times 10^{-4} (\varepsilon_{pr})^{-3.078} \quad \text{when } \varepsilon_{pr} \geq 0.00863 \quad (8)$$

$$N = 0.12 (\varepsilon_{pr})^{-1.867} \quad \text{when } \varepsilon_{pr} < 0.00863 \quad (9)$$

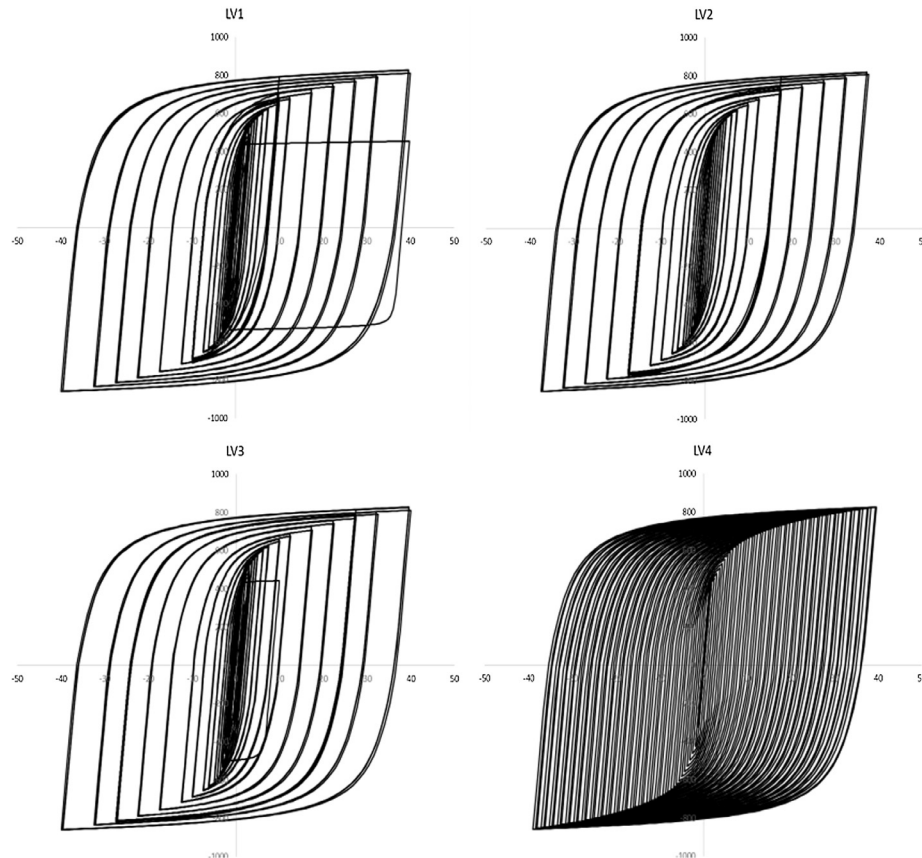


Fig. 8. Hysteresis loops of numerical simulation for specimens subjected to LV1 to LV4 (LYS).

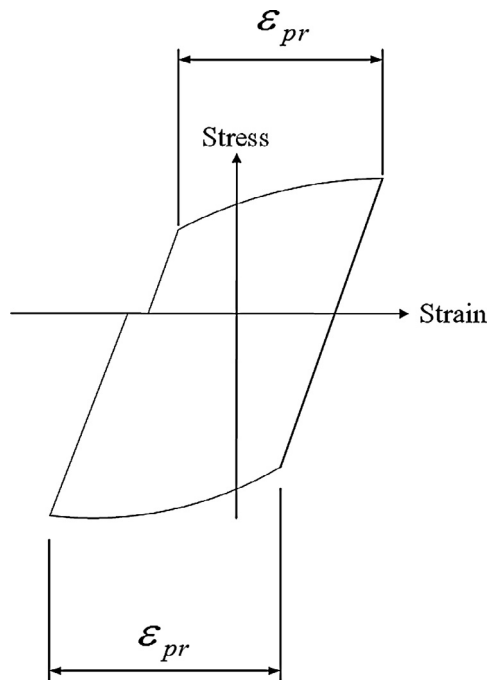


Fig. 9. Illustration of plastic strain range.

Table 2
BRB damage index via simulation.

	LV1	LV2	LV3	LV4	Ave.
Damage index	1.25	0.85	0.94	1.07	1.03

in which ε_{pr} is the plastic strain range of one half cycle, as shown in Fig. 9. The parameter N is the number of cycles to cause fatigue failure corresponding to ε_{pr} . Table 2 shows the damage index for LYS-BRB by numerical simulation. Because the number of specimens is insufficient, the values of damage index shown in Table 2 deviate from the reference value (i.e., 1.0) to a certain degree. Nevertheless, these values are considerably closer to the expected value, indicating that the linear Miner cumulative index (M-index) provides an acceptable prediction.

4. Numerical studies

4.1. Structural configuration, loading and design requirements

As shown in Fig. 10, the demonstrated building is a 20-story steel moment frame with a floor plan of 5×3 bays, in which an equal bay spacing of 9 m is used. Except for the first floor, which has a story height of 4.5 m, the story height of the remaining floors is 4 m [13]. The BRB in the demonstrated building is arranged based on engineering practice. For example, the number of BRB in the lower stories is often greater than that of the higher stories. In addition, an open space is usually provided in the middle span of the outer frame. Therefore, for stories that are less than twelve story, the BRBs are installed on the two side spans of the outer frame along the X direction, and the second and fourth spans on the inner frames along the Y direction. For stories that are greater than twelve story, the number of BRB decreases from two to one in both X and Y directions as indicated in Figs. 10.1–10.3, respectively. Two types of columns are used: C1 connected to braces and C2 unconnected to braces. The floors are 12 cm in thickness and are fabricated with 4000 psi concrete.

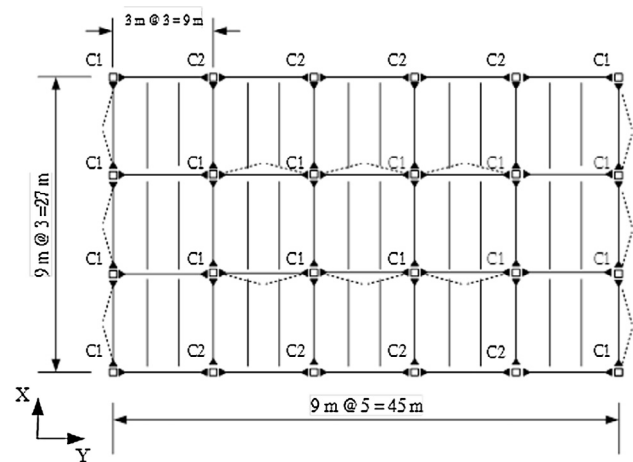


Fig. 10.1. Plan view of the studied frame.

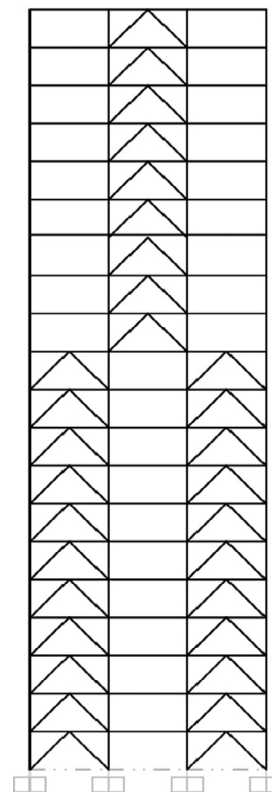


Fig. 10.2. Elevation view of the 20-story building in X direction.

The static load is 1.1 tf/m² for floors 1 to 7, 1.0 tf/m² for floors 8 to 14 and 0.9 tf/m² for floors 14 to roof. The live load is 0.2 tf/m² for floors 1 to 19 and 0.3 tf/m² for the roof. The total weight of the structure is approximately 24421.5 ton. It is assumed that the building is located in Zone II of Taipei and the buildings are designed for a peak ground acceleration (PGA) of 0.291 g based on a Taiwan seismic hazard curve corresponding to a 10% exceedance probability in 50 years. The design criteria are:

1. Under the design earthquake, the maximum inter-story drift of the buildings may not exceed the 0.5% limit.
2. The strength ratio of column, beam and brace must be less than 0.95.

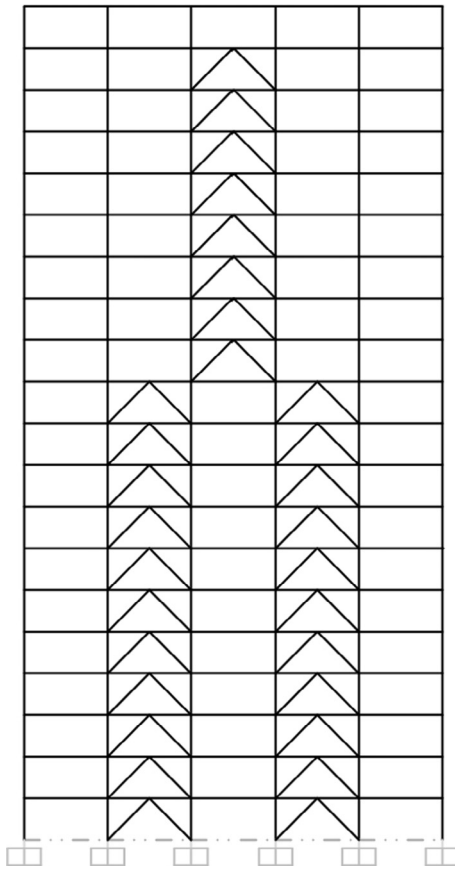


Fig. 10.3. Elevation view of the 20-story building in Y direction.

3. The moment structure should be able to sustain 25% seismic force alone.
4. The depth of the beams may not be less than 1/20 of the span.
5. Beams in both directions beams are separately designed. Ideally, the beam depth should be identical in both directions. In case they are different, the differential may not be smaller than 10 mm to facilitate installation of the stiffener inside the box-type columns.

4.2. Preliminary designs and materials

In the preliminary study, three buildings are designed under the same criteria (section 4.1) and are termed SNSN, SNHT and HTHT.

Table 3

Periods of three preliminary buildings.

	SNSN	SNHT	HTHT
1st period	2.56 s	2.68 s	2.84 s
2nd period	2.49 s	2.56 s	2.70 s
3rd period	1.81 s	1.88 s	1.95 s

Table 4

Mechanical properties for the steel materials used in case study.

Steel	Yield stress (N/mm ²)				Ultimate stress (N/mm ²)
SN490B	6 ≤ t ≤ 12 325	12 ≤ t ≤ 16 325–445	16 ≤ t ≤ 40 325–445	t > 40 295–415	490–610
SN490C	16 ≤ t ≤ 40 325–445	40 ≤ t ≤ 50 295–415	t > 50 295–415		490–610
A36	300				400–550
HT690	550				690

SNSN indicates SN490 is used for both beam and column, and SNHT indicates that SN490 and HT690 are used for beam and column, respectively. HTHT indicates that HT690 is used for both beam and column. For a fair comparison, these three buildings are designed to have a similar strength ratio. Nonetheless, there are some exceptions. For example, the depth of beams is strictly not permitted to be less than 1/20 of the span by Taiwan practices. In such a situation, the strength ratio may not be the major controlling factor, making it impossible for all three buildings to have an identical strength ratio. One of the focuses in these preliminary designs is to identify the performance of the SNSN building that is used as the design target (or constraints) in the subsequent optimization study. Please note that in practice, the built-up box is often used for columns and all beam-to-column joints are designed as moment-resisting connections in Taiwan.

The core material in BRB is A36. The minimum cross-section area for the braces is 30 cm² with an increment of 5 cm². SN 490 and HT 690 are used for beam and column, respectively. If the plate thickness of the beams is larger than 40 mm, the material is changed from SN490B to SN490C and a uniform girder size is used for all stories (BH400 × 300 × 12 × 25). Periods of the three buildings are displayed in Table 3. As expected, the HTHT frame has a lower stiffness as a result of the smaller section and therefore has the highest period. Table 4 shows the properties of SN490B, SN490C, HT690 and A36 steel.

4.3. Evaluation process

Both static and dynamic analyses are conducted in the structural evaluation process. The key evaluations in the static analysis are inter-story drift, strength ratio and whether the moment-resisting frame has the ability to sustain 25% of the seismic force without the presence of the BRB. The key evaluations in the dynamic analysis are inter-story drift, top-floor acceleration amplification factor and maximum/cumulative damage index of the BRB. For dynamic analysis, the design regulations in Taiwan require a minimum of three earthquake records, and their response spectrums must be scaled to fit the design response spectrum. To be specific, for a damping ratio of 5%, the response spectrum of the selected earthquakes falling in between 0.2 T and 1.5 T (T as the fundamental period) may not be lower than 90% of the corresponding design spectral acceleration. In addition, the average value of the response spectrum within the designated period range may not be lower than the average value of the corresponding design spectral accelerations. This study selects eight seismic records and scales them based on the above regulations, as shown in Fig. 11.

4.4. Results of static analysis for the preliminary buildings

Table 5 displays the maximum inter-story drifts of these three buildings. As expected, to satisfy the demands of gravity loading, the SNSN frame needs to have a greater column size because its material strength is lower than others, resulting to a greater structural stiffness and a smaller inter-story drift.

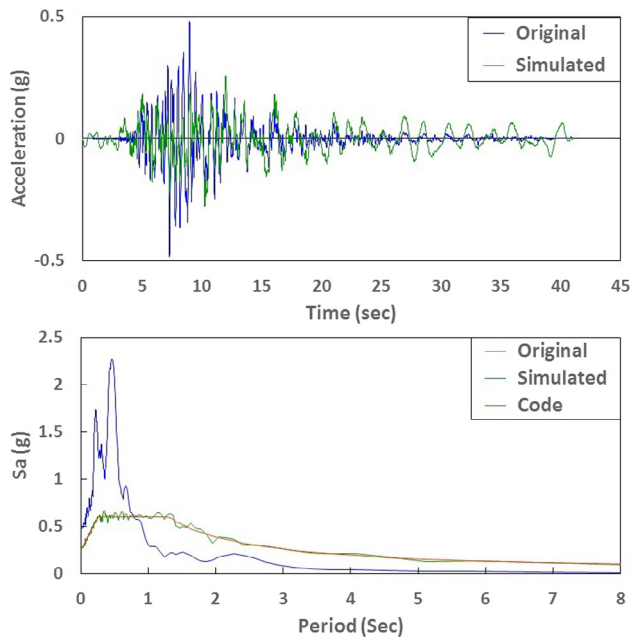


Fig. 11. Example of the Kobe earthquake and the scaled spectrum compatible with the design spectrum of 475 years.

Table 5
Maximum inter-story drifts (%) of the three buildings under static analysis.

Frame	X-Dir.	Y-Dir.
SNSN	0.38%	0.33%
SNHT	0.45%	0.39%
HTHT	0.46%	0.48%

Table 6
Total steel weight used in the three buildings.

Frame	Total steel content (Ton)	Reduction rate ^a
SNSN	3720	–
SNHT	3310	11.01%
HTHT	2986	19.71%

^a Compared to SNSN

Table 7
Strength ratios of the three moment resisting frames under 25% seismic loading.

Frame	Strength ratio of beam	Strength ratio of column
SNSN	0.3–0.65	0.3–0.45
SNHT	0.35–0.55	0.35–0.75
HTHT	0.3–0.45	0.25–0.7

Although the inter-story drifts of SNHT and HTHT frames are not up to the level of SNSN, they still meet the requirements (0.5%). Note that the BRBs in these three buildings are at the same locations but have different section areas. Table 6 shows the total steel weight used in these three buildings. Compared to the SNSN frame, the HTHT and SNHT frames can reduce the total steel weight by 19% and 11%, respectively. Table 7 displays the strength ratios of three buildings only with a moment resisting

frame (i.e., no BRB) under 25% seismic loading, indicating that all three buildings meet the standards.

4.5. Results of dynamic analysis for the preliminary buildings

Eight sets of earthquake records are selected from the NGA-West2 Ground Motion Database, namely TCU065, TCU084, TCU129, CHY028, TAP103, Kobe, Loma Prieta and Northridge. Fig. 11 displays the time history and response spectrum of the scaled Kobe earthquake corresponding to the 475-year design response spectrum. The PGAs of all of the scaled earthquakes are shown in Table 8.

Fig. 12 shows the X direction inter-story drift of each floor for three buildings under the scaled Kobe earthquake excitation. It is seen that for all buildings, the BRB arrangement has a significant influence on the drift values. For example, the inter-story drifts between the 11th and 12th stories are abruptly heightened because of the reduced number of braces (from 2 to 1) on the 12th floor.

Table 9 exhibits the maximum inter-story drift of three buildings for the eight earthquake excitations in both directions. Similar to the results of static analysis, the SNSN frame has the smallest inter-story drift. Analysis of variance (ANOVA) is adopted to analyze the inter-story drift performance among three buildings. As indicated in Table 9, the difference among them is significant. Nevertheless, the inter-story drifts of three buildings all meet the requirement of collapse prevention in FEMA356 (2%).

To evaluate the fatigue performance for three buildings, the fatigue damage index (M-index) is used. Two types of M-index are used as the measurement for comparison: the maximum value of M-index among all BRB members in a building (denoted as Dmax hereafter) and the cumulative value of M-index for all BRB members in a building (denoted as Cdamage hereafter). Table 10 shows the Dmax in X direction and the corresponding story number for three buildings. It is seen that Dmax is prone to occur on higher stories because of the vertical layout of BRB. Table 11 shows the Cdamage in the X direction. The results of ANOVA show that differentials in X-axis Dmax among the three buildings are not significant, but that the differentials in Y-axis Dmax, X-axis Cdamage and Y-axis Cdamage are significant. The all-steel BRB of all three buildings has not yet reached fatigue failure point under the selected earthquake excitations. Among them, the BRB of the SNSN frame absorbs the highest level of energy and SNHT follows.

The “roof acceleration amplification factor” refers to the max ratio of the roof acceleration to the ground acceleration through the entire dynamic analysis duration. Table 12 shows the X-axis (in positive direction) roof acceleration amplification factor of the three buildings under the eight sets of scaled seismic excitations. The results indicate that the roof acceleration amplification factors of all three building all meet the code requirement. In addition, the F value suggests that the differentials among the three buildings in terms of roof acceleration factor are not significant.

4.6. Optimal design using PSO and its structural responses

To increase the benefits and structural performance of using high-strength steel, this study used PSO to find an optimized design (O_SNHT) having the equivalent structural performance of an SNSN

Table 8
PGA of the eight scaled earthquakes.

Earthquake	TCU065	TCU084	TCU129	TAP103	CHY028	Kobe	Loma Prieta	Northridge
PGA (g)	0.34	0.26	0.30	0.31	0.26	0.27	0.25	0.26

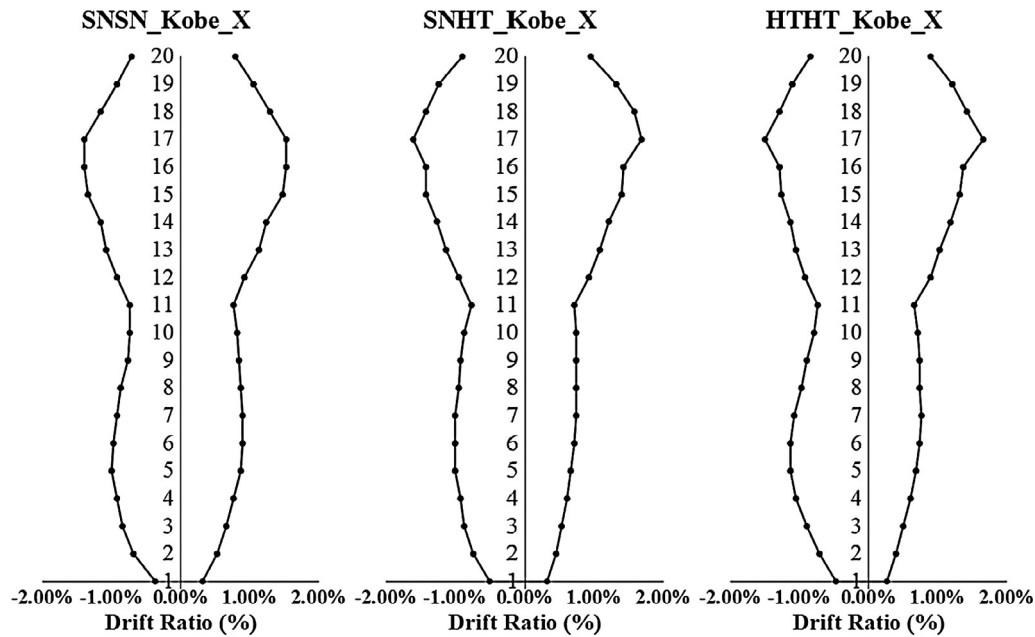


Fig. 12. X-Dir. inter-story drifts under the scaled Kobe earthquake excitation.

Table 9

Maximum inter-story drifts of three buildings for the eight earthquakes.

	X-direction			Y-direction		
	D_SNSN	D_SNHT	D_HTHT	D_SNSN	D_SNHT	D_HTHT
TCU065	1.27%	1.50%	1.93%	1.42%	1.35%	1.63%
TCU084	1.29%	1.62%	1.62%	1.24%	1.41%	1.35%
TCU129	1.17%	1.36%	1.32%	1.14%	1.31%	1.34%
TAP103	1.35%	1.83%	1.84%	1.28%	1.54%	1.59%
CHY028	1.29%	1.56%	1.57%	1.13%	1.33%	1.45%
Kobe	1.53%	1.66%	1.64%	1.44%	1.59%	1.66%
LomaPrieta	1.56%	1.65%	1.57%	1.40%	1.59%	1.62%
Northridge	1.34%	1.77%	1.65%	1.17%	1.47%	1.44%
Average	1.35%	1.62%	1.64%	1.28%	1.45%	1.51%
STD	0.00132	0.001487	0.00184	0.00128	0.00115	0.00130
ANOVA	F value	8.62		7.46		
	Critical value	3.47		3.47		

Table 10

Dmax in X direction for three buildings.

	SNSN	Story	SNHT	Story	HTHT	Story
TCU065	0.0035	16	0.0023	13	0.0021	17
TCU084	0.0036	16	0.0035	17	0.0031	17
TCU129	0.0034	16	0.0013	17	0.0011	17
TAP103	0.0026	16	0.0028	17	0.0028	17
CHY028	0.0023	16	0.0023	17	0.0021	17
Kobe	0.0031	16	0.0027	17	0.0023	17
LomaPrieta	0.0031	16	0.0029	17	0.0026	17
Northridge	0.0030	17	0.0043	17	0.0041	17
Average	0.0031		0.0028		0.0025	
STD	4.46×10^{-4}		8.86×10^{-4}		8.73×10^{-4}	
ANOVA	F value	1.045				
	Critical value	3.466				

frame that is confirmed by dynamic and fragility analysis. In addition, the strength ratios of the each element in the optimization design are suggested as a design reference for engineers. Factors considered in the optimization process include the following: maximum inter-story drift should be no greater than the maximum inter-story drift of SNSN frame, BRB strength ratio must fall between 0.95 and

0.7 and the column size in lower floors may not be smaller than that in higher floors. The design variables are the width and thickness of box column and BRB core area. Because the column size is designed with two floors in a unit, the number of design variables is 79. It should be noted that the dynamic analysis is not included in optimization because of its higher computational cost.

Table 11
Cdamage in X direction for three buildings.

	SNSN	SNHT	HTHT
TCU065	0.12	0.10	0.10
TCU084	0.14	0.11	0.11
TCU129	0.14	0.04	0.04
TAP103	0.13	0.09	0.09
CHY028	0.07	0.05	0.05
Kobe	0.13	0.01	0.01
LomaPrieta	0.13	0.11	0.11
Northridge	0.10	0.11	0.10
Average	0.121	0.077	0.076
STD	0.0239	0.0388	0.0377
ANOVA	F value	4.247	
	Critical value	3.466	

Table 12
X-axis top-level acceleration amplification factor (positive).

Earthquake	SNSN	SNHT	HTHT
TCU065	2.2	2.3	2.2
TCU084	3.0	3.3	3.2
TCU129	2.1	2.1	2.3
TAP103	2.2	2.2	2.1
CHY028	3.0	2.9	2.7
Kobe	2.4	2.4	2.3
LomaPrieta	3.2	3.2	3.2
Northridge	3.1	3.1	3.3
Average	2.6	2.7	2.7
STD	0.46	0.49	0.50
ANOVA	F value	0.012	
	Critical value	3.466	

In summary, the optimization is displayed in Eq. (10):

Min. the total weight of building

$$s.t. \begin{cases} \text{story drift} \leq \text{Maximum story drift of SNSN} \\ \text{column size}_i \geq \text{column size}_{i+1} \\ 0.7 \leq \text{Brace stress ratio} \leq 0.95 \\ \text{particle lower bound} \leq \text{particle (section size)} \\ \leq \text{particle upper bound} \\ \text{stress ratio of beam and column} \leq 0.95 \end{cases} \quad (10)$$

where i is the story number from 1 to 20

In the optimization process, a parametric structural model is developed for evaluating the building responses in an automatic fashion. The SAP2000 Application Programming Interface (API) is able to carry out both pre- and post-processing such as assigning the section area and capturing the strength ratio, respectively. Thus, the API is adopted here to prepare the building model and deliver the analysis and design outcomes in each optimization iteration. PSO is used as the optimization engine by taking advantage of not being trapped in a local minimum because of the inherent random searching procedure. A new position of a particle, which represents a set of section sizes in the current study, is generated using Eq. (11), as shown below:

$$\bar{x}_i(t+1) = \bar{v}_i(t+1) + \bar{x}_i(t) \quad (11)$$

where $\bar{x}_i(t+1)$ denotes the position of the i^{th} particle in the next iteration, $\bar{x}_i(t)$ denotes the position of the i^{th} particle in the current iteration and $\bar{v}_i(t+1)$ denotes the velocity of the i^{th} particle in the current iteration. The velocity of the i^{th} particle is determined by Eq. (12), as shown below:

$$\bar{v}_i(t+1) = w \times \bar{v}_i(t) + r_1 c_1 (\bar{x}_{pBest} - \bar{x}_i(t)) + r_2 c_2 (\bar{x}_{gBest} - \bar{x}_i(t)) \quad (12)$$

where w is the inertia factor, $\bar{v}_i(t)$ is the velocity of at previous iteration, r_i ($i = 1-2$) are random numbers between 0 and 1, and c_1 and

Table 13
Parameters of PSO used in this study.

Number of particle	10
Number of iteration	40
Column width upper bound	1500
Column width lower bound	100
Column thickness upper bound	70
Column thickness lower bound	16
BRB area upper bound	300
BRB area lower bound	10
Upper bound of w	0.9
Lower bound of w	0.2
c_1	2
c_2	2

c_2 are the cognition factor and the social factor, respectively. The parameter \bar{x}_{pBest} is the particle position with the minimum objective value in the i^{th} population, and \bar{x}_{gBest} is the particle position with the minimum objective value among all populations. Detailed information for the PSO used here can be found in Table 13. The flowchart of PSO-based optimization is shown in Fig. 13.

Fig. 14 shows the convergence history of the objective function. The maximum X-axis inter-story drift of the O_SNHT frame is 0.38% (SNSN: 0.38%), and the maximum Y-axis inter-story drift is 0.32% (SNSN: 0.33%). The total steel weight for O_SNHT is 3211 tons, which achieves a saving of 13% steel compared to that of SNSN frame. It can be observed that the proposed optimization algorithm reduces the inter-story drift (from 0.45% to 0.38% and from 0.39% to 0.32% for the X-axis and Y-axis, respectively) as well as the amount of steel. Based on the analysis results of O_SNHT, the strength ratios of C1 and C2 columns, beams and braces are recommended to be the vicinities of 0.9, 0.8, 0.8 and 0.95, respectively, to ensure that the design frame fits the concept of damage control.

Although the dynamic analysis is not included in optimization, the performances of the optimal frame (O_SNHT) under seismic excitations are examined and displayed in Table 14. Compared to the results of SNSN, inter-story drifts and top-floor acceleration amplification factors of O_SNHT in both X and Y directions are similar to those of SNSN. In the BRB damage index, significant differences are found in all indices except Y-axis Dmax. It is seen that although the dynamic analysis is not considered in optimization, most of the indices indicate that the structural performance of O_SNHT is similar to that of SNSN. Please note that all responses of O_SNHT meet the standards.

4.7. Results of fragility analysis

In addition to evaluate the deterministic performance of the investigated buildings, this study further assessed the probabilistic performance of two frames, O_SNHT and SNSN, through the fragility analysis. In general, the inter-story drift is used as the structural performance index, and therefore the relationship between spectral acceleration and maximum inter-story drift is established through Eq. (13).

$$D = a(S_a)^b \quad (13)$$

in which D is the demand of the inter-story drift, S_a is the spectral acceleration and a and b are constants derived from regression analysis.

The fragility curve is a conditional probability computation, representing a system failure probability for a given intensity measurement. For example, when S_a is given, assuming that the capacity and demand of the building are lognormally distributed, the corresponding failure probability can be calculated through Eq. (14):

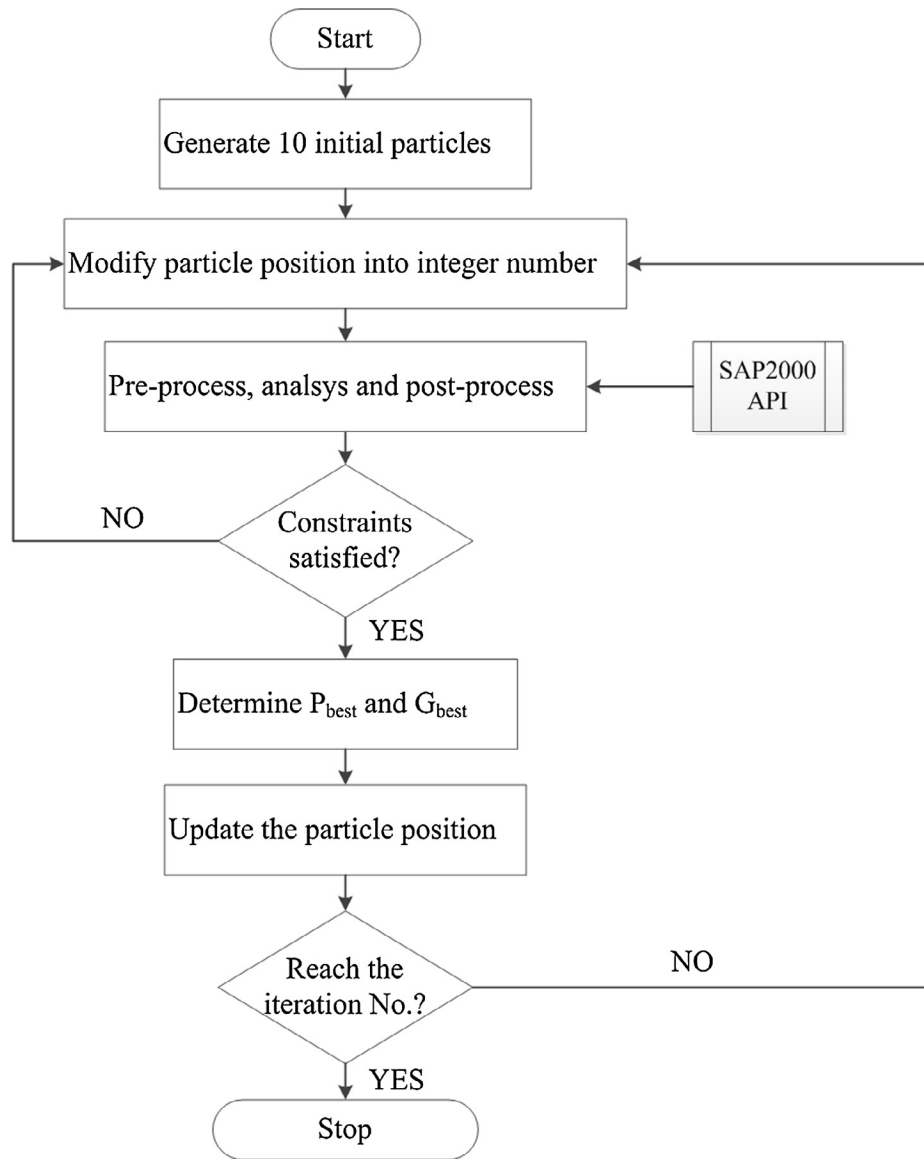


Fig. 13. Flow chart of PSO-based optimization.

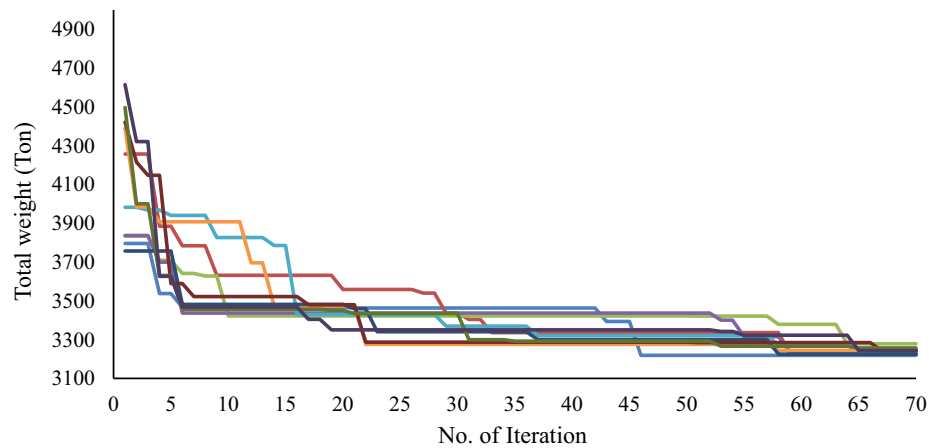


Fig. 14. History of O_SNHT objective function values.

Table 14
Dynamic performance comparison between O_SNHT and SNSN frames.

		O_SNHT	SNSN
X_drift	Average	1.31%	1.35%
	STD	0.0006	0.00132
	Z-value	0.79 (1.96)	
Y_drift	Average	1.17%	1.28%
	STD	0.0011	0.00128
	Z-value	1.81 (1.96)	
X_Dmax	Average	0.0020	0.0031
	STD	0.0013	0.00043
	Z-value	2.25 (1.96)	
Y_Dmax	Average	0.0029	0.0028
	STD	0.0009	0.00048
	Z-value	1.64 (1.96)	
X_Cdamage	Average	0.05	0.12
	STD	0.03	0.02
	Z-value	5.38 (1.96)	
Y_Cdamage	Average	0.06	0.15
	STD	0.03	0.04
	Z-value	4.77 (1.96)	
X-axis top-floor acceleration amplification factor (positive)	Average	2.6	2.6
	STD	0.56	0.47
	Z-value	0.21 (1.96)	
X-axis top-floor acceleration amplification factor (negative)	Average	2.5	2.4
	STD	0.24	0.27
	Z-value	0.43 (1.96)	
Y-axis top-floor acceleration amplification factor (positive)	Average	2.8	2.8
	STD	0.63	0.40
	Z-value	0.19 (1.96)	
Y-axis top-floor acceleration amplification factor (negative)	Average	2.6	2.5
	STD	0.40	0.43
	Z-value	0.54 (1.96)	

$$P_f(C > D | S_a = x) = 1 - \phi \left[\frac{\ln(\frac{C}{D})}{\beta} \right] = 1 - \phi \left[\frac{\ln(\frac{C}{ax^b})}{\beta} \right] \quad (14)$$

in which C is the mean value of the capacity, $D(a(S_a)^b)$ is the mean value of demand in terms of inter-story drift, is the standard deviation with respect to the limit state, and is the probability density function of standard normal. With reference to the FEMA356, two structural performance levels are adopted: life safety (LS) and collapse prevention (CP). That is, the values of C are 1.5% and 2% for LS and CP, respectively. The parameter is calculated by Eq. (15):

$$\beta = \sqrt{\beta_{D|S_a}^2 + \beta_c^2} \quad (15)$$

in which c is the standard deviation of capacity for a given S_a . The value falls between 0.2 and 0.4 [14]. The parameter $\beta_{D|S_a}$ is the standard deviation of demand corresponding to a given S_a , representing the uncertainty in inter-story drift under excitations with a given S_a . To calculate the value of $\beta_{D|S_a}$, similar to D , this study establishes the relationship between the standard deviation of the inter-story drift and spectral acceleration from eight sets of earthquake excitations and from Eq. (16), as shown below.

$$\beta_{D|S_a} = c(S_a)^f \quad (16)$$

in which c and f are constants derived from regression analysis. Parameters of a , b , c , and f are displayed in Table 15.

Table 15
Parameters used in fragility analysis.

Regression parameter	O_SNHT	SNSN
a	3.65	3.84
b	0.932	0.924
c	0.37	0.43
f	0.960	0.986

Fig. 15 shows the fragility curves of O_SNHT and SNSN (COV of capacity are 0.2, 0.3 and 0.4) targeting on the performance levels of LS and CP. It is seen that the trends of LS and CP fragility curves of the two buildings are similar. When S_a is larger than 0.8 g - 1.2 g, the fragility curve of O_SNHT rises gradually above that of the SNSN frame. In other conditions, the performance of O_SNHT frame is slightly better than the SNSN frame. Although dynamic analysis is not part of the optimization, the results show that the structural

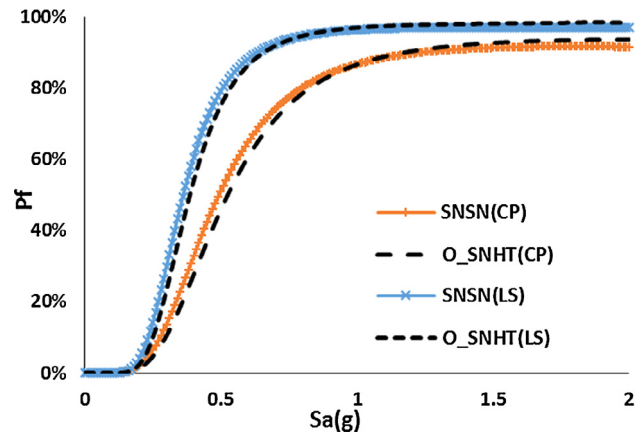


Fig. 15.1. Fragility curves for O_SNHT and SNSN with COV of 0.2.

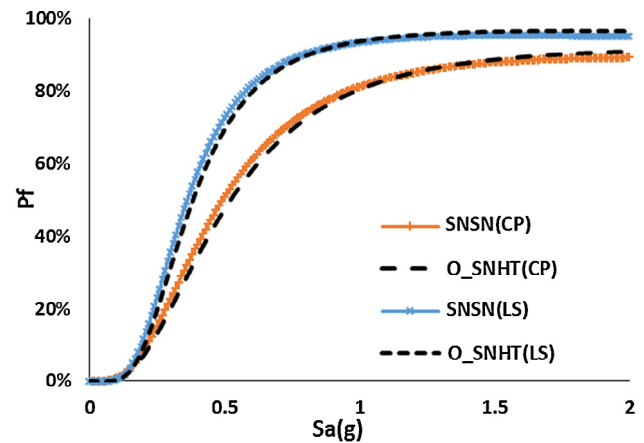


Fig. 15.2. Fragility curves for O_SNHT and SNSN with COV of 0.3.

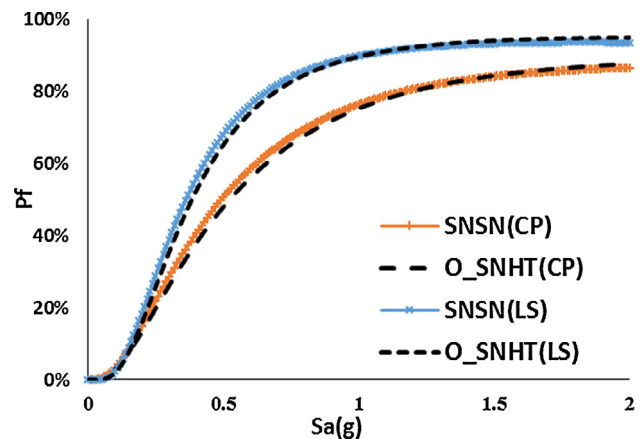


Fig. 15.3. Fragility curves for O_SNHT and SNSN with COV of 0.4.

performance of the optimal frame (O_SNHT) is indeed fairly close to the performance of SNSN.

5. Conclusion

This study explored the safety and economic benefits of a dual-steel moment frame constructed using a combination of high-strength and high-ductility steel. An ABAQUS UMAT was established to simulate the BRB nonlinear behavior based on test results. The all-steel BRB damage index was investigated through Miner's suggestion [12]. Three numerical examples, based on 20-story dual-steel moment frames (SNSN, SNHT and HTHT) located in Zone II Taipei, were used to obtain detailed information with respect to the issues of safety and economic cost. To ensure that damage occur in the brace system first, different strength ratio are assigned for the main and secondary systems in the design stage. Pseudo-static, dynamic and fragility analyses were conducted to compare the structural performances among three frames using ANOVA. The structural performances investigated included the inter-story drift, maximum roof acceleration, property of BRB hysteresis, strength ratio between main frame and BRB and cumulative fatigue damage. To ensure that the SNHT structure can provide similar structural performance as structures built with regular steel but with minimized use of steel materials, a PSO-based optimization was carried out. Fragility analyses confirmed that the structural performance of the optimization design was similar to the SNSN frame. From the results of the abovementioned analyses, it was found that all structures constructed from regular or high-strength steel met the standards in both static and dynamic analysis. Compared to SNSN, SNHT saved 11% steel; however, the dynamic analysis indicated that control of the maximum inter-story drift of SNHT was not as favorable as SNSN. After performing optimization, O_SNHT saved approximately 13% of steel compared to SNSN and simultaneously improved the structural performance of SNHT up to the level comparable with SNSN or even higher. The fragility curve of O_SNHT was similar to that of SNSN in both LS and CP. In particular, if the spectrum acceleration is smaller than 0.8 g, O_SNHT is more capable in terms of satisfying the demands in LS and CP. Based on the results of optimization, for a 20-story dual-steel moment frame, the strength ratios of C1 and C2 columns, beams and braces are recommended to be the vicinities of 0.9, 0.8, 0.8 and 0.95, respectively, to ensure that the designed frame can provide similar performance to the optimal design identified in this study.

Conflict of interest

No conflict of interest.

Acknowledgements

The authors would like to thank the China Steel Corporation (Taiwan) for financially supporting this study.

Appendix A: Establishment of the hysteretic model

The two bounding surfaces method is combined with kinematic hardening to form the complete hysteretic modeling as described below.

1. For $i = 1$ to the required increment number,

$$\Delta S = E\Delta\varepsilon; \sigma^{i+1} = \sigma^i + \Delta S; \alpha^i = E_p^i \varepsilon^p$$

where i is the i^{th} increment, is the strain increment, E is the elastic modulus, S is the stress increment, σ^i is the stress at i^{th} increment, is the shifted stress value, E_p^i is the strain-hardening parameter at the i^{th} increment, and ε^p is the accumulated plastic strain.

2. If status(i) = elastic, perform the following calculations:

```

If  $|\sigma^{i+1} - \alpha| \leq \sigma_y r$ 
 $\sigma^{i+1} = \sigma^{i+1}$ 
else
  status( $i + 1$ ) = yielded
   $\beta = \frac{\sigma_y - |\sigma^i - \alpha^i|}{|\sigma^{i+1}| - |\sigma^i - \alpha^i|}$ 
  End if
else
  go to step 3
end if

```

3. If status (i) = yielded, perform the following calculations:

```

If  $\sigma^i \Delta s < 0$ 
  status( $i + 1$ ) = elastic
   $\sigma^{i+1} = \sigma^{i+1}$ 
else
   $\beta = 0$ 
  End if
else
  go to step 4
End if

```

4. Compute

$$\sigma^{i+1} = \sigma^i + \beta \Delta S + \frac{EE_p^i}{E + E_p^i} (1 - \beta) \Delta \varepsilon$$

$$\varepsilon^p = \varepsilon^p + \frac{1 - \beta}{1 + E_p^i/E} \Delta \varepsilon$$

5. Compute

$$E_p^{i+1} = E_p^0 + (E - E_p^0) \times \left(\frac{\delta^i}{\delta_{in}^i} \right)^2$$

6. If $\sigma_a < \sigma_s$

```

 $|B_s^{n+1}| = |B_s^{n+1}| + 2\Delta s F_h$ 
else
 $|B_s^{n+1}| = |B_s^{n+1}| - 2\Delta s F_s$ 
End if

```

where B_s^n is the stress bound in the i^{th} increment, Δs is $|\sigma_s - \sigma_a|$, F_h is the hardening coefficient and F_s is the softening coefficient.

7. End for

References

- [1] J. Zhang, T. Zirakian, Probabilistic assessment of structures with SPSW systems and LYP steel infill plates using fragility function method, *Eng. Struct.* 85 (2015) 195–205.
- [2] A. Tenchini, M. D'Aniello, C. Rebelo, R. Landolfo, L.S. Silva, L. Lima, Seismic performance of dual-steel moment resisting frames, *J. Constr. Steel Res.* 101 (2014) 437–454.

- [3] F. Perri, C. Faella, E. Martinelli, Cost-competitive hysteretic devices for seismic energy dissipation in steel bracings: experimental tests and low-cycle fatigue characterization, *Constr. Build. Mater.* 113 (2016) 57–67.
- [4] J.D. Marshall, F.A. Charney, Seismic response of steel frame structures with hybrid passive control systems, *Earthq. Eng. Struct. D* 41 (2012) 715–733.
- [5] V. Budaházy, L. Dunai, Numerical analysis of concrete filled Buckling Restrained Braces, *J. Constr. Steel Res.* 115 (2015) 92–105.
- [6] N. Hoveidae, R. Tremblay, B. Rafezy, A. Davarand, Numerical investigation of seismic behavior of short-core all-steel buckling restrained braces, *J. Constr. Steel Res.* 114 (2015) 89–99.
- [7] C.C. Chen, S.Y. Chen, J.J. Liaw, Application of low yield strength steel on controlled plastification ductile concentrically braced frames, *Can. J. Civ. Eng.* 28 (2001) 823–836.
- [8] J. Bai, J. Ou, Earthquake-resistant design of buckling-restrained braced RC moment frames using performance-based plastic design method, *Eng. Struct.* 107 (2016) 66–79.
- [9] N.G. Cofie, H. Krawinkler, Uniaxial cyclic stress-strain behavior of structural steel, *J. Eng. Mech.* 111 (1985) 1105–1120.
- [10] C.H. Wang, Behavior of Buckling Inhibited Braces and seismic performance of the ductile concentrically braced frame system. PhD. Thesis of NTUST 2002, Taipei, Taiwan.
- [11] H.I. Ling, H.B. Liu, Y. Mohri, T. Kawabata, Bounding surface model for geosynthetic reinforcements, *J. Eng. Mech.* 127 (9) (2001) 963–967.
- [12] M.A. Miner, Cumulative damage in fatigue, *J. Appl. Mech.* 12 (1954) 159–164.
- [13] K.C. Lin, C.C.J. Lin, J.Y. Chen, H.Y. Chang, Seismic reliability of steel framed buildings, *Struct. Saf.* 32 (2010) 174–182.
- [14] K.W. Liao, Y.K. Wen, D.A. Foutch, Evaluation of 3-D steel moment frames under earthquake excitations. II reliability and redundancy, *J. Struct. Eng.* 133 (3) (2007) 471–480.